Received: 17 March 2020 | Revised: 10 May 2020 | Accepted: 24 May 2020

DOI: 10.1002/inf2.12155

WILEY

SPECIAL ISSUE ARTICLE

Band structure engineering through van der Waals heterostructing superlattices of two-dimensional transition metal dichalcogenides

Xin-Gang Zhao[1] | **Zhiming Shi**[2] | **Xinjiang Wang**[3] | **Hongshuai Zou**[1] | **Yuhao Fu**[3] | **Lijun Zhang**[1]

[1] State Key Laboratory of Integrated Optoelectronics, Key Laboratory of Automobile Materials of MOE, College of Materials Science and Engineering, Jilin University, Changchun, Jilin, China

[2] State Key Laboratory of Luminescence and Applications, Changchun Institute of Optics, Fine Mechanics and Physics, Chinese Academy of Sciences, Changchun, Jilin, China

[3] College of Physics, Jilin University, Changchun, Jilin, China

Correspondence
Lijun Zhang, State Key Laboratory of Integrated Optoelectronics, Key Laboratory of Automobile Materials of MOE, College of Materials Science and Engineering, Jilin University, Changchun 130012, China.
Email: lijun_zhang@jlu.edu.cn

Funding information
Jilin Province Science and Technology Development Program, Grant/Award Number: 20190201016JC; National Natural Science Foundation of China, Grant/Award Numbers: 61722403, 11674121

Abstract

The indirect-to-direct band-gap transition in transition metal dichalcogenides (TMDCs) from bulk to monolayer, accompanying with other unique properties of two-dimensional materials, has endowed them great potential in optoelectronic devices. The easy transferability and feasible epitaxial growth pave a promising way to further tune the optical properties by constructing van der Waals heterostructures. Here, we performed a systematic high-throughput first-principles study of electronic structure and optical properties of the layer-by-layer stacking TMDCs heterostructing superlattices, with the configuration space of $[(MX_2)_n–(M'X'_2)_{10-n}]$ ($M/M' =$ Cr, Mo, W; $X/X' =$ S, Se, Te; $n = 0$-10). Our calculations involving long-range dispersive interaction show that the indirect-to-direct band-gap transition or even semiconductor-to-metal transition can be realized by changing component compositions of superlattices. Further analysis indicates that the indirect-to-direct band-gap transition can be ascribed to the in-plane strain induced by lattice mismatch. The semiconductor-to-metal transition may be attributed to the band offset among different components that is modified by the in-plane strain. The superlattices with direct band-gap show quite weak band-gap optical transition because of the spacial separation of the electronic states involved. In general, the layers stacking-order of superlattices results in a small up to 0.2 eV band gap fluctuation because of the built-in potential. Our results provide useful guidance for engineering band structure and optical properties in TMDCs heterostructing superlattices.

KEYWORDS

heterostructures, indirect-to-direct band-gap transition, superlattices, transition metal dichalcogenides, two-dimensional materials

---

Xin-Gang Zhao and Zhiming Shi contributed equally to this study.

1 | INTRODUCTION

Two-dimensional (2D) transition metal dichalcogenides (TMDCs) monolayers, with X—M—X triple atoms, present extremely strong light-matter interactions due to the direct optical band gap in the near-infrared to visible spectral range (0.7-2.0 eV).[1-4] Hence, TMDCs are highly expected to apply in electronic transistor,[5] optical catalysis,[6] and solar cell[7,8] due to the suitable band gap, high on/off ratio,[5] strong photoluminescence,[9-11] and high conductivity.[12] However, the optoelectric response intensity for the direct band-gap single-layer MoS_2 and WS_2 is quite low by comparing to their bulk systems. But the bulk TMDCs exhibit indirect band-gap.

Many efforts were donated by the scientists to optimize/tune the electronic band structure of single/few layers of TMDCs, such as applying external electric field,[13-17] in-plane (uniaxial or biaxial) strain,[18-29] and constructing heterostructures.[17,30-37] Lu et al reported that the electric field induced dipole moment should be responsible to the underlying directbandgap in heterostructures.[26] Biaxial strain can induce the transition from direct to indirect bandgap for monolayer TMDCs,[18,19,24] but does not work in bulk TMDCs.[32] Yun et al showed that semiconducting of MoS_2, $MoSe_2$, and $MoTe_2$ transfers into metallic as the external biaxial strain is larger than 9.8%, and the direct bandgap can just tolerate biaxial strain within −1.3% to 5%.[18] The excellent transferability of TMDCs allows the band structures engineering via constructing van der Waals (vdW) heterostructures.[38] The heterostructures not only significantly improve the absorption comparing to the monolayer,[39] facilitate the eletron-hole separation in different layers,[30,32-37] but also have the possibilities to inherit the direct bandgap from monolayer, such as vdW TMDCs heterostructures,[37] and MoS_2/graphene heterostructures.[30] Kou et al. explained the inner-plane strain due to lattice mismatch and the polarization at interface can significantly tune the bandgap values that in the few layered heterostructures $(MoX_2)_n(MoY_2)_m$ (X, Y = S, Se, Te).[17] Especially, the interface polarization can be sensitively tuned by excess electric field, which can result in semiconductor-to-metal transition but no indirect-to-direct transition. The density of functional theory (DFT) calculations reveal that the applied in-plane strain on MoS_2—MX_2 superlattices can also widely tuned the band gap.[40] However, the in-plane strain on superlattices of MX_2 are rarely studied,[41] though there are intensive studies on the few layers heterostructures.[30-37,40,42] The superlattices consist of periodic stacking of very thin alternating layers of two different TMDCs, which are distinct from the few layers heterostructures. Note that combination of two different 2D semiconductor to form superlattices or heterostructures, the intrinsic band offset,[38] and built-in layer-thickness[43] due to different stacked order play important roles to tune the bandgap values.[44,45] The former usually leads to lower bandgap than the bandgap of homogenous 2D semiconductor,[17,42] while the later can lead to varying of bandgap values[46] though it is generally uncontrollable in experiment.

In this work, we present a computational study of tuning electronic band structures via constructing TMDCs heterostructing superlattices $[(A)_n—(B)_{10-n}]$ (A, $B = MX_2$; M = Cr, Mo, W; X = S, Se, Te). We systematically studied three types of heterostructing superlattices (type A: A and B with same transition metal M but different chalcogen X, type B: A and B with same chalcogen X but different transition metal M, type C: A and B with different transition metal M and chalcogen X), within 10-layer periodic unit cell (Figure 1A). The evolution of band structures, including indirect-to-direct bandgap transition, semiconductor-to-metal transition as the content of MX_2 and $M'X'_2$ is revealed. A direct/indirect bandgap fluctuation due to different built-in layer thickness because of variation of the layers stacking order of superlattices is also observed. Further analysis of the results indicates the factors that are responsible for the above observations including the band offset among different components and the in-plane strain caused by the lattice mismatch.

2 | COMPUTATIONAL APPROACH

Our calculations are performed within the framework of DFT using the plane-wave pseudopotential implemented in the Vienna Ab initio Simulation Package (VASP).[47,48] The electron-core interactions are described with the frozen-core projector-augmented pseudopotential. The generalized gradient approximation formulated by Perdew, Burke, and Ernzerhof (PBE)[49] is used as the exchange correction. The equilibrium structural parameters including the lattice constants and internal coordinates are obtained by using total energy minimization via conjugate-gradient algorithm. The vdW interactions are included for geometrical optimization by DFT-D2 method.[50] The kinetic energy cutoff for S, Se, Te, Cr, Mo, W are set to 364, 276, 228, 295, 292, and 290 eV. The electronic configurations for S, Se, Te, Cr, Mo, and W elements are $3s^23p^4$, $4s^24p^4$, $5s^25p^4$, $3d^54s^1$, $4d^44s^2$, and $4d^44s^2$. The k-point meshes with grid spacing of $2\pi \times 0.015$ Å^{-1} is used for electronic Brillouin zone integration. As shown in Table S1, the calculated lattice constants of bulk 2H-MX_2 agree well to the experimental values.

The electronic band structures are calculated by using PBE functional without including the spin-orbit coupling

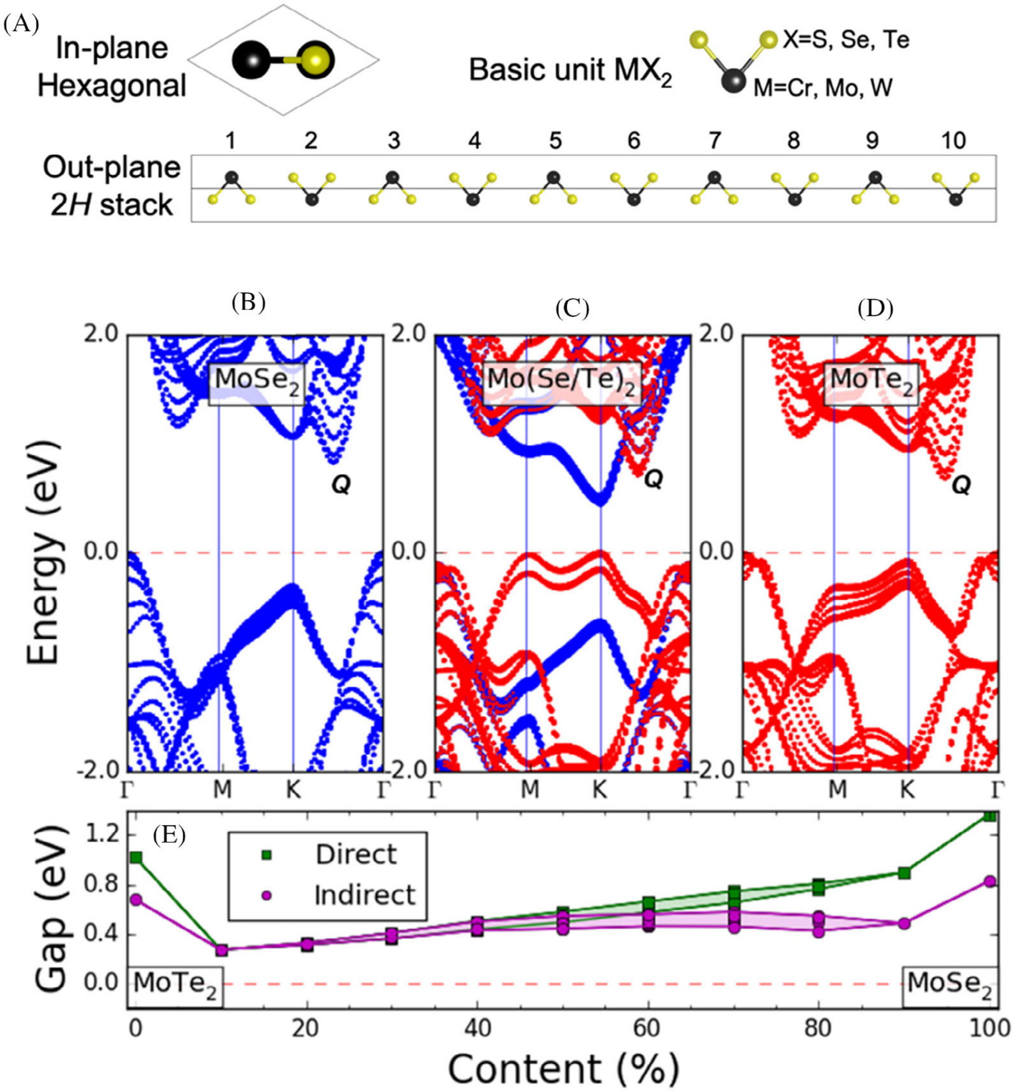

FIGURE 1 A, Schematics of (in-/out-plane views and the basic unit) 10-layer unit cell to constructing heterostructing superlattice. Band structures of, B, homogenous $MoSe_2$ 10-layered supercell, C, $[(MoSe_2)_2$—$(MoTe_2)_8]$ heterostructing superlattice, and, D, homogenous 10-layered $MoTe_2$ supercell. The "*Q*" points in B,D refer to the conduction band minimum (CBM) for the bulk structures. E, Direct/indirect bandgap depends on the content (ie, $n/10$) of $MoSe_2$ in $[(MoSe_2)_n$—$(MoTe_2)_{10-n}]$. The filled areas reflect the fluctuations of band gap values induced by stacked orders

(SOC) and electronic dispersion interaction among interlayer.[4,51,52] Since the SOC can result in bandgap splitting up to 400 meV in $2H$-MX_2 with inversion symmetry.[53-55] The strong excitonic effect in MX_2 also contributes to the red shift of band gap.[27] Standard DFT functionals show reasonable bandgap values (see Table S1), which is due to the accidental cancellation between the underestimation of bandgap values[56] with the standard DFT functional and SOC effect and the actual excitonic effect captured by the experimental optical measurements.[27]

The $[(MX_2)_n$—$(M'X'_2)_{10-n}]$ heterostructing superlattices of different TMDCs materials are optimized by using same parameter for optimization and keeping the initial symmetry. A series of bilayer MoS_2, $MoSe_2$, $MoTe_2$ with continuously variable in-plane strain are selected to only optimize internal atomic coordination with parameter sets for superlattice optimization. Their band edges are evaluated by PBE functional and discussed in Section 2. Creation of calculation workflows, management of large amounts of calculations, extraction of calculated results, and post-processing analysis are performed by using an open-source Python framework designed for large-scale high-throughput energetic and property calculations, JUMP[2] (to be released soon).

3 | RESULTS AND DISCUSSION

3.1 | Electronic band structure of TMDCs heterostructing superlattices

To meet the computational cost of structural optimization and exploring the bandgap evolution of heterostrucuting superlattice, as shown in Figure 1A, we used a 10-layer heterostructing superlattice $[(A)_n—(B)_{10-n}]$ (no vacuum layer; A and B referring to the basic units MX_2; n = 0-10) as the unit cell. The most stable AB-stacking pattern (ie, *2H* phase) that has be found experimentally[57-59] (see in-plane and out-plane in Figure 1A) is adopted for all the studied systems. For each $[(A)_n—(B)_{10-n}]$ system, there are 128 possibilities for different stacked orders when n varies from 0 to 10. Totally, we construct 1024 configurations and group them into three types: type A $[(MX_2)_n—(MX'_2)_{10-n}]$ (3*128 = 384) with same transition metal and different chalcogen X, type B $[(MX_2)_n—(M'X_2)_{10-n}]$ (3*128 = 384) with different transition metal and same chalcogen X, and type C $[(MX_2)_n—(M'X'_2)_{10-n}]$ (2*128 = 256) with different transition metal M and chalcogen X. We consider monolayer MX_2 (ie, MX_2 = MoS_2, $MoSe_2$, $MoTe_2$, WS_2, WSe_2, WTe_2, CrS_2, $CrSe_2$, and $CrTe_2$) as basic units to construct heterostructing superlattices within 10-layer unit cell, $[(A)_n—(B)_{10-n}]$, where n is the number of one of the units MX_2. Among the constituting basic units, the *2H*-phase MoS_2, $MoSe_2$, $MoTe_2$, WS_2, and $MoSe_2$ have been synthesized in experiment,[57-59] whereas CrS_2, $CrSe_2$, $CrTe_2$, and WTe_2 are assumed as the *2H*-phase to investigate the whole trend of electronic band structure variation in the TMDCs heterostructing superlattices. Besides, because of structural similarities between MoX_2 and WX_2, we expect similar electronic and mechanical behaviors. All the configurations are optimized (including the lattice constant and interatomic position) by constraining to initial group symmetry. Then we collect the band structures for all of superlattice configurations for further analysis.

3.1.1 | Type A heterostructing superlattices $[(MX_2)_n—(MX'_2)_{10-n}]$

Three kind of combinations, $[(MoS_2)_n—(MoSe_2)_{10-n}]$, $[(MoSe_2)_n—(MoTe_2)_{10-n}]$ and $[(MoS_2)_n—(MoTe_2)_{10-n}]$ heterostructing superlattices are studied. The electronic band structures of homogenous 10-layers stacked $MoSe_2$ and $MoTe_2$ are displayed in Figure 1B,D. The valence band maximum (VBM) locate at Γ points, and conduction band minimum (CBM) locates at the middle of K-Γ path, defined as Q point, revealing that both bulk $MoSe_2$ and $MoTe_2$ are with indirect bandgap, agreeing with experimental observations.[18] In contrast, as shown in Figure 1C, the 10-layered $[(MoSe_2)_2—(MoTe_2)_8]$ heterostructing superlattice presents direct bandgap at K point. This demonstrates the indirect-to-direct bandgap transition from homogeneous layered bulk materials to heterostructing superlattices. As shown in Figure 1E, the heterostructing superlattices $[(MoSe_2)_n—(MoTe_2)_{10-n}]$ exhibit direct bandgaps by 0.27 and 0.32 eV when $n = 1$ and $n = 2$. Yet, the direct bandgaps are slightly higher than the indirect band gaps for $n = 0$ to 3 and get closer to each other by increasing the content ($n/10$) of $MoSe_2$. This implies that the heterostructing superlattices with few layers of $MoSe_2$ possess small gaps and occur indirect-to-direct bandgap transition. From Figure 1E, we find that the bandgap fluctuations up to 0.1 eV induced by different built-in layer thickness, indicating that the indirect-to-direct bandgap transition is not sensitive to stacked orders.

By analyzing the projected band structure of $[(MoSe_2)_2—(MoTe_2)_8]$ in Figure 1C, we can find the CBM is contributed by $MoSe_2$ (blue dots) and the VBM is contributed by $MoTe_2$ (red dots). This implies the electron-hole separation at band edges, which is consistent with the previous findings in TMDCs heterostructures.[30,32-37]

We plot the corresponding ratio of the configurations with direct bandgap (or metallic property) over total of 128 configurations as R_d (or R_m) in Figure 2 for each type of superlattices. Detailed results are listed in Table S2. For $[(MoSe_2)_n—(MoTe_2)_{10-n}]$ heterostructing superlattices, R_d is equal to 18.5%, but no metallic configuration is obtained. Though $[(MoS_2)_n—(MoSe_2)_{10-n}]$ heterostructing superlattices are all with the indirect bandgap, and the band gap values of the superlattices gradually decrease by

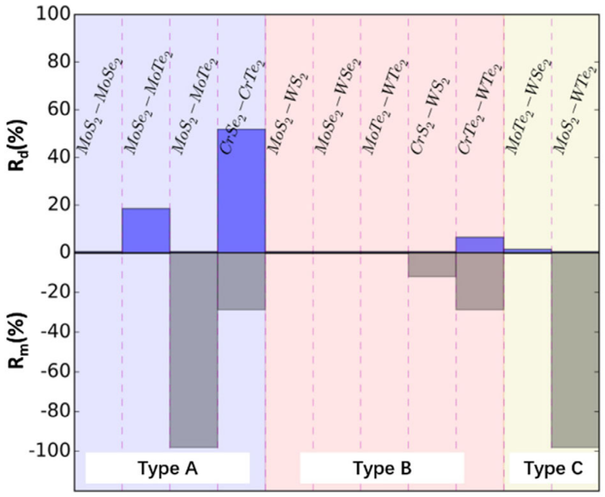

FIGURE 2 The crossover percentage of transitions for indirect-to-direct bandgap (R_d, blue bars), and for semiconductor-to-metal (R_m, gray bar). The blank areas represent no transitions

reducing MoS_2 content (Figure 3A). And all of $[(MoS_2)_n—(MoTe_2)_{10-n}]$ superlattices are metallic (Figures 2 and 3C). Besides, we find $R_d = 51.9\%$ and $R_m = 28.7\%$ for $[(CrSe_2)_n—(CrTe_2)_{10-n}]$ heterostructing superlattices (Figures 2 and S1).

3.1.2 | Type B heterostructing superlattices $[(MX_2)_n—(M'X_2)_{10-n}]$

Here we consider three kinds of type B superlattices including $[(MoS_2)_n—(WS_2)_{10-n}]$, $[(MoSe_2)_n—(WSe_2)_{10-n}]$, and $[(MoTe_2)_n—(WTe_2)_{10-n}]$, aiming to figure out the effects of cations on band gaps. As shown in Figure 3D, the indirect and direct bandgap values for $[(MoS_2)_n—(WS_2)_{10-n}]$ heterostructing superlattices are in the range of 0.73-0.94 and 1.30-1.41 eV, respectively, when n = 1-9. For all of type B superlattices, their direct bandgap values are always larger than the corresponding indirect bandgaps, demonstrating no indirect-to-direct bandgap transition. The corresponding indirect and direct bandgaps are not sensitive to contents n, which is different from type A heterostructing superlattices. By increasing the atomic number of anions in $[(MoX_2)_n—(WX_2)_{10-n}]$ heterostructing superlattices (ie, X changes from S to Te), only the indirect bandgaps are smaller than that in homogenous configurations, as shown in Figure 3D,F. However, neither indirect-to-direct bandgap transition nor semiconductor-to-metal transition is observed in three type B heterostructing superlattices. Moreover, in $[(MoX_2)_n—(WX_2)_{10-n}]$ heterostructing superlattices, the VBM is at Γ point, and CBM at Q point, which is analogous to the homogenous stacked bulk MX_2 (Figure 1A,C). Besides, we also calculate the indirect and direct bandgap values of all configurations of $[(CrTe_2)_n—(WTe_2)_{10-n}]$ heterostructing superlattices and show them in Figure 2. We find 6.5% configurations of $[(CrTe_2)_n—(WTe_2)_{10-n}]$ heterostructing superlattices occur indirect-to-direct bandgap transition, and 2.8% configurations of $[(CrTe_2)_n—(WTe_2)_{10-n}]$ heterostructing superlattices are metallic compounds.

3.1.3 | Type C heterostructing superlattice $[(MX_2)_n—(M'Y_2)_{10-n}]$

Here, we only consider two kinds of type C heterostructing superlattice in this family, i.e, $[(WSe_2)_n—(MoTe_2)_{10-n}]$ and $[(MoS_2)_n—(WTe_2)_{10-n}]$. As shown in Figure 2, the 2.8% configurations of $[(WSe_2)_n—(MoTe_2)_{10-n}]$ superlattices present indirect-to-direct bandgap transition, and 92.6% configurations become metallic compounds. While except the

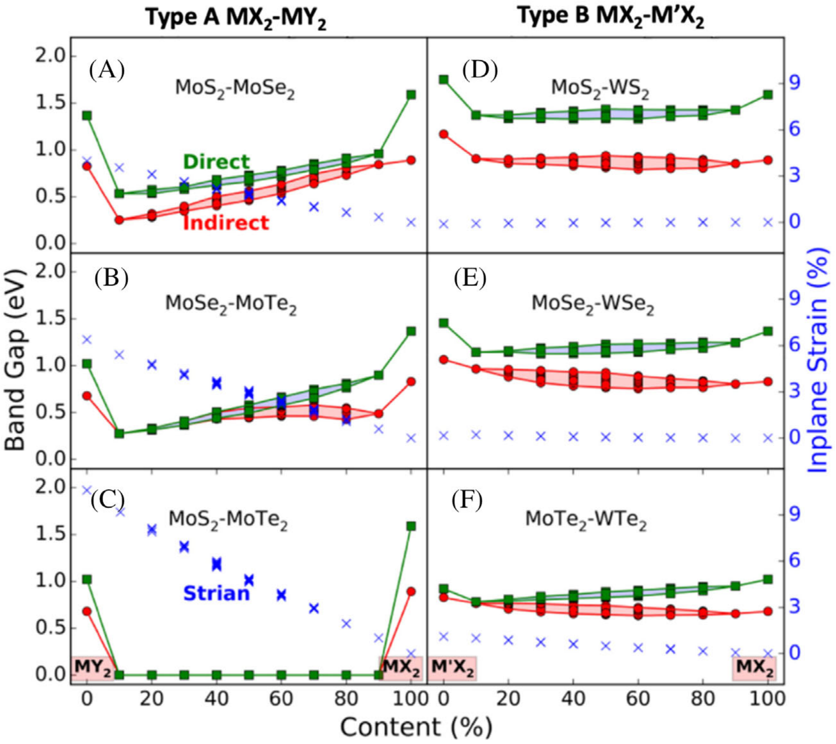

FIGURE 3 Band gaps of type A and type B superlattice as the function of content n (indirect bandgap: red circle lines, direct bandgap: green square lines). The in-plane strain respect to bulk MX_2 are also depicted (blue cross). The filled areas reflect the fluctuations of bandgaps due to different stacked orders

homogenous stacked WS_2 and $MoTe_2$, all the heterostructing superlattice configurations turn to be metallic for type C $[(MoS_2)_n$—$(WTe_2)_{10-n}]$ superlattice. Apparently, we can conclude that the semiconductor-to-metal transition mainly depends on the differences of the anion, though the band edges are dominated by the *d* orbitals of cations.

3.2 | Physical mechanism underlying semiconductor-metal and indirect-to-direct bandgap transitions

3.2.1 | Band offsets leading to band gap reduction

We define the band offset as the absolute value of the sum of relative shift of band edges between any two homogenous 10-layered slabs (depicted in Figure 4). The VBM of 10-layered $MoTe_2$ at Γ point is set to zero. The energy level of VBM located at Γ point for other MX_2 refers to the energy level of VBM of 10-layered $MoTe_2$ slab. The CBM locates at *Q* point (the middle point along *K* to Γ, see Figure 1A), which is consistent with bulk MX_2. As shown in Figure 4, the band offset without considering lattice mismatch are 0.30, 0.54, and 0.24 eV for MoS_2—$MoSe_2$, MoS_2—$MoTe_2$, $MoSe_2$—$MoTe_2$, and 0.42, 0.35, and 0.34 eV for MoS_2—WS_2, $MoSe_2$—WSe_2, $MoTe_2$—WTe_2, respectively. Note that the VBM and CBM energy levels for MX_2 in Table S3 refer to the core level (S-1*s*), which also reveals consistent of band offset trends using 10-layered or Monolayer MX_2 slab. Consequently, the band offset can induce the bandgap reduction (Figure 3) by constructing TMDCs heterostructures.[60] Note that the band offset for $MoTe_2$—WSe_2 is 0.38 eV, but is 1.28 eV for MoS_2—WTe_2 (Table S4).

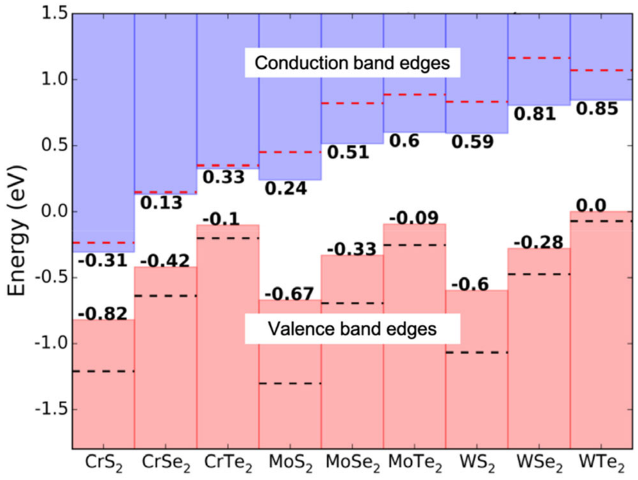

FIGURE 4 Relative valence band maixmum (VBM) and conduction band minimum (CBM) energy levels of MX_2 with respect to vacuum level. The VBM of 10-layered $MoTe_2$ slab was set to zero. The VBM and CBM energy levels for single-layer MX_2 (dash lines) with respect to 10-layer $MoTe_2$ slab were also plotted as references

3.2.2 | In-plane strain caused by lattice mismatch resulting in band edge shift

As we mentioned above, we do not consider the lattice mismatch for all three types of superlattices. Here, we collect the in-plane strain for type A and type B as shown in Figure 3 (blue cross symbols). The smallest in-plane lattice constant of the building unit is adapted as the reference. Indeed, the type A heterostructing superlattices with significant bandgap shift exhibit large in-plane strain (>3%). However, the in-plane strain is less than 1% due to the similar radius of anion X in type B heterostructing superlattices, which might moderately contribute to the change of band gap.

To identify the effect of in-plane strain on the electronic band structure, we firstly calculated the band structure of bilayer MoS_2 slab under positive in-plane strain (from 1% to 8%). From Figure 5, the CBM locates at *K* point, the VBM always locates at Γ point. By rising in-plane strain, we find the bandgap values decrease and conduction band edges at *K* point and *Q* point gradually shift down. Note that two broaden bands at *Q* point approaches to be degenerate when the applied strain reaches to 8%. This agrees with Ellis' finding,[61] in which they suggested that the strong splitting in the conduction band of multilayers MoS_2 along *K*-Γ path shifts down relative to the *K*-point minimum, leading to an indirect band gap respect to monolayer MoS_2. And the band edges shift is not a unique property for homogenous bilayer MX_2. In heterostructure, such as $[(WSe_2)_n$—$(MoS_2)_{10-n}]$ can also found the VBM transition from *K* to Γ due to external strain, leading to indirect gap.[17,26] Therefore, we might qualitative figure out the effect on electronic structure in heterostructing superlattices because of in-plane strain analogous to the in-plane strain on layered slabs.

Then, as shown in Figure 6, we calculated band edges shift respect to the vacuum level by applying in-plane strain on bilayer MoS_2, $MoSe_2$, and $MoTe_2$ slabs. One can find that the valence band edges at *K*, *M*, and *Q* points for bilayer MoS_2, $MoSe_2$, and $MoTe_2$ gradually shift down as the in-plane strain changing from −7% to +7%. The slopes for *K*, *M*, and *Q* as the function of in-plane are similar, which may originate the same M-$d_{x2\text{-}y2}$ and Mo-d_{xy} orbital contribution (Table S5). In contrast, the valence band edge at Γ point contributed by Mo-d_{z2}, d_{xz}, and d_{yz} orbitals shifts up (Figure 6A,C,E). The converse tendency may attribute

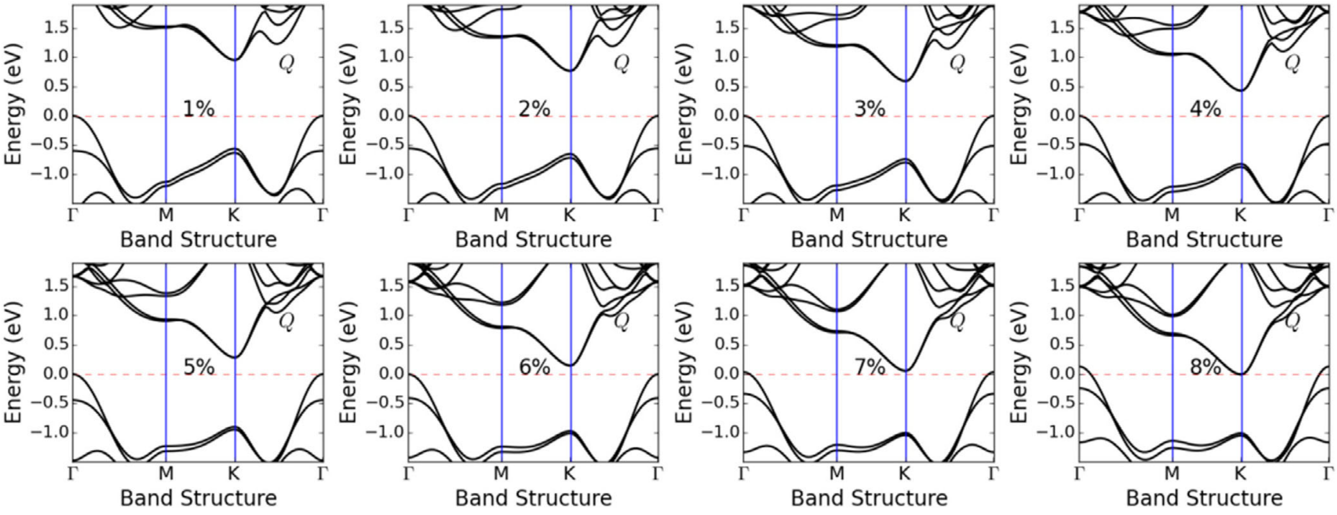

FIGURE 5 Band edges shift for bilayer MoS_2 slab by applying in-plane strain (ie, lattice expansion along a and b vectors) from 1% to 8%. The conduction band minimum (CBM) in the crystalline MoS_2 was addressed as *Q* point

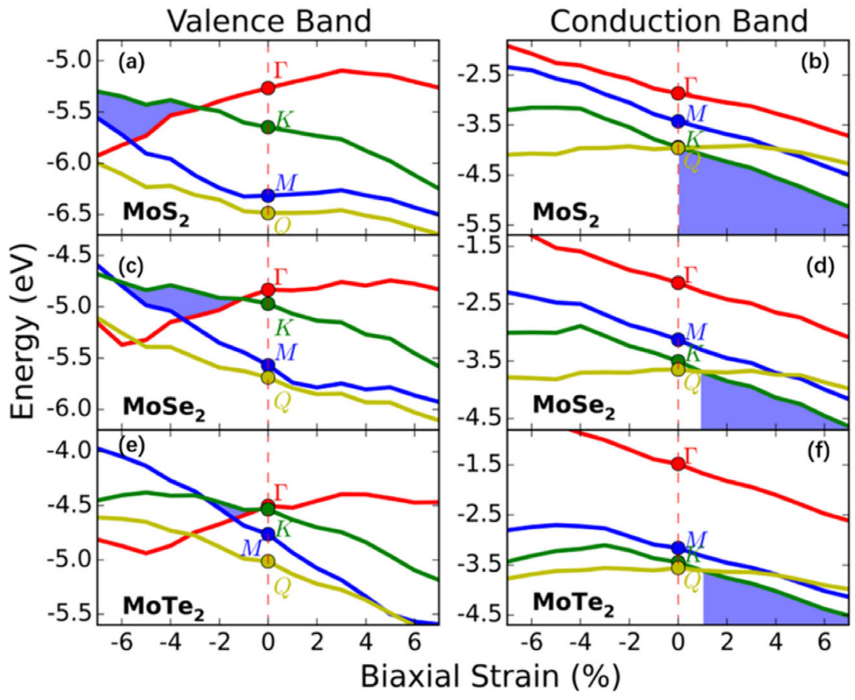

FIGURE 6 Band edge shifts at special k-points, that is, *Γ*, *K*, *M*, and *Q* (red/green/blue/yellow) in bilayer MoS_2, A,B, $MoSe_2$, C,D, and $MoTe_2$, E,F slabs against to applied biaxial in-plane strain. The blue shadowed areas refer to the valence band maximum (VBM) or conduction band minimum (CBM) that would shift to K

to the strong anti-bonding states at *Γ* point comparing with the non-bonding or weak bonding states away from *Γ* point (*M*, *K*, *Q* points). The VBM always locates at *Γ* point by applying tensile strain, same as the results in Figure 5. For the conduction band edge (Figure 6B,D,F), the *Γ*, *K*, *M*, *Q* points gradually decrease as the in-plane strain rising from −7% to +7%. The VBM for bilayer MoS_2, $MoSe_2$ and $MoTe_2$ slabs always occurs at *Q* point when applying compressive strain, and the tensile strain results in the transition from *Q* to *K* points. Overall, to achieve the direct bandgap heterostructing superlattices, we should combine two TMDCs with moderate in-plane strain. Quantitively, the blue shadowed region in Figure 6 refers to the band edges that occur at *K* points under in-plane strain. The area of the shadowed region enclosed by lines of *Γ*, *K*, *M* shrinks as the atomic number of S > Se > Te for both valence and conduction band edges. The conduction band edges can be easily tuned to K point by applying less than 1% in-plane strain for bilayer MoX_2 (X = S, Se and Te). Note that MoSe_2 and MoTe_2 are the optimal building units for achieving the VBM at K point within applying moderate in-plane strain (less 2% compression), comparing to MoS_2. Indeed, we find that (see Figure 2) $[(\mathrm{MSe}_2)_n\text{—}(\mathrm{MTe}_2)_{10-n}]$ heterostructing superlattices are the optimal combination for achieving direct bandgap configurations in type A and type C. Therefore, we can conclude that the intrinsic in-plane strain due to lattice mismatch accounts for the indirect-direct bandgap transition as well as the semiconductor-to-metal transition.

To further confirm the in-plane strain effect on bandgap evolution due to lattice mismatch, we select $[(\mathrm{CrTe}_2)_n\text{—}(\mathrm{WTe}_2)_{10-n}]$ heterostructing superlattices, in which the lattice mismatch between is larger than that in $[(\mathrm{MoS}_2)_n\text{—}(\mathrm{MoSe}_2)_{10-n}]$ and $[(\mathrm{MoSe}_2)_n\text{—}(\mathrm{MoTe}_2)_{10-n}]$ heterostructing superlattices depicted in Figure 2. Both indirect-to-direct bandgap and semiconductor-to-metal transitions are found. In contrast, the absence of in-plane strain due to lattice mismatch (<1%) between MX_2 and $M'X_2$ would not induce indirect-to-direct bandgap transition in type B (Figure 2). The $[(\mathrm{CrS}_2)_n\text{—}(\mathrm{WS}_2)_{10-n}]$ heteostructing superlattice shows semiconductor-to-metal transition, which might be collaboratively affected by large band offset and small in-plane strain. In fact, as shown in Figure 2, type C superlattices exhibit metallic property. Their in-plane strain is within range of 3.17% to 11.56%. This further demonstrates the band edges shift are induced by in-plane strain effect.

3.2.3 | Different built-in potential in heterostructing superlattices results in the bandgap fluctuation

As shown in Figure 3A,B,D-F, the direct bandgap and indirect bandgap values distribute in a range (ca. 0.2 eV) for the superlattices $[(A)_n\text{—}(B)_{10-n}]$ with given n $(1 < n < 9)$ as well as shown in Figure S1. It is well known that the built-in potential in heterostructures such as graphene/WS_2,[62] can be formed due to hetero-stacking, which can be considered as the spontaneous vertical electric filed.[14] Note that Liu et al find that the band gap of the bilayer MoS_2 monotonically depends on the external vertical electric field.[14] Here, given n in heterostructing superlattice $[(A)_n\text{—}(B)_{10-n}]$, there are different stacked orders, leading to different built-in potential, which further results in variation of bandgap values. In addition, the ubiquitous interlayer coupling effect in the multiple layered 2D materials[4,51,63-65] may also contribute to the band gap variation. In Figure S2, we show the averaged built-in potential along layer-stacking direction based on two of configurations of heterostructing superlattice $[(\mathrm{MoSe}_2)_5\text{—}(\mathrm{MoTe}_2)_5]$ with different stacking order (ie, ABABABABAB and AAAAABBBBB). Although the charge mainly distributes on the MoTe_2 layers (Figure S2), the built-in potential for ABABABABAB stacked configuration fluctuates in short range, the AAAAABBBBB stacked configuration presents two apparent ranges, which depends on the thickness of the homogenous layers.[17] Consequently, the former has bandgap 0.72 eV, which is larger than the later (0.42 eV).

3.3 | Optical absorption spectra of the heterostructing superlattices with direct bandgap

We explore the optical properties of the configurations in heterostructing superlattices with direct bandgap, including $[(\mathrm{CrSe}_2)_n\text{—}(\mathrm{CrTe}_2)_{10-n}]$, $[(\mathrm{CrTe}_2)_n\text{—}(\mathrm{WTe}_2)_{10-n}]$, $[(\mathrm{MoSe}_2)_n\text{—}(\mathrm{MoTe}_2)_{10-n}]$, and $[(\mathrm{WSe}_2)_n\text{—}(\mathrm{MoTe}_2)_{10-n}]$ superlattice to study the optical absorption. From Figure 7, we can find that optical absorption of mixed compounds stronger than that of silicon crystalline in range of low photonic energy, which reaches maximum at 1.5 eV. However, $[(\mathrm{CrSe}_2)_n\text{—}(\mathrm{CrTe}_2)_{10-n}]$, $[(\mathrm{CrTe}_2)_n\text{—}(\mathrm{WTe}_2)_{10-n}]$, $[(\mathrm{MoSe}_2)_n\text{—}(\mathrm{MoTe}_2)_{10-n}]$, and

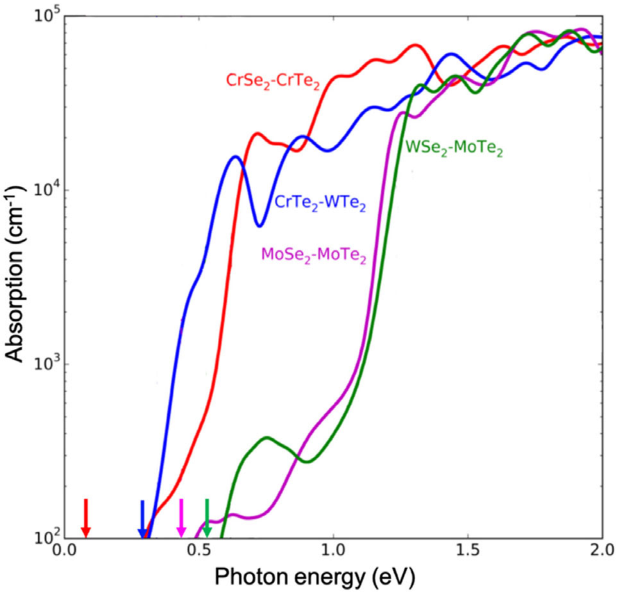

FIGURE 7 Optical absorption spectra of selected heterostructing superlattices with direct band gap ($[(\mathrm{CrSe}_2)_n\text{—}(\mathrm{CrTe}_2)_{10-n}]$, $[(\mathrm{CrTe}_2)_n\text{—}(\mathrm{WTe}_2)_{10-n}]$, $[(\mathrm{MoSe}_2)_n\text{—}(\mathrm{MoTe}_2)_{10-n}]$ and $[(\mathrm{WSe}_2)_n\text{—}(\mathrm{MoTe}_2)_{10-n}]$). The vertical arrows refer to the direct gap of the corresponding systems in the same color

$[(WSe_2)_n–(MoTe_2)_{10-n}]$, the optical absorption is negligible at the position of direct band gap. This is because of electron-hole spacial separation (see Figure 1C), in which no wavefunction hybridizations between different layers. The implication is that the exciton lifetime in heterostructing superlattices with direct bandgap should be much longer than that in homogenous MX_2,[65-67] which maybe potential materials for solar cell or charge transport devices. However, these superlattice with direct bandgap might be not good emitters due to charge special separation, which may have low quantum yield.[68]

4 | CONCLUSIONS

We systematically studied the evolution of electronic structures and optical property for TMDCs heterostructing superlattices $[(MX_2)_n(M'X'_2)_{10-n}]$ within 10-layer unit cell (M/M′ = Cr, Mo, W; X/X′ = S, Se, Te; n = 0-10) by using high-throughput first-principle calculations. Our calculated results reveal that the indirect-direct bandgap transition (Γ-Q to K-K) or even semiconductor-to-metal transition can be realized by changing component compositions of superlattices. The bandgap fluctuation caused by the layer stacked orders of superlattices is small (up to 0.2 eV) because of the built-in potential. Further analysis implies that the indirect-direct bandgap transition is originated from the in-plane strain induced by lattice mismatch. The band offsets among different components that is modified by the in-plane strain contribute to the semiconductor-to-metal transition. Moreover, we find that the superlattices with direct bandgap show negligible band edges optical transition because of the spatial separation of the electronic states on different MX_2 layers.

It should be pointed out that in this work we did not consider the small lattice mismatch between the different basic units MX_2 during the construction of TMDCs heterostructing superlattices. This means the two MX_2 units were forcedly compressed/stretched to form a common lattice, where the residual forces are coherently relaxed across the interface between two MX_2 units. In the real experiment, the weak vdW interaction among the sublayers of heterostructures/superlattices may not be strong enough to form a coherence lattice. The superlattices or heterostructures with the small lattice mismatch may form a periodic Moiré superlattice pattern,[69-71] which can result in substantial bandgap modulation. Nevertheless, our results give useful guidance for engineering band structure and optical properties in TMDCs out-of-plane heterostructing superlattices and may provide a specific database for further studying band gap evolution of TMDCs heterostructing superlattice by using machine learning approach.

ACKNOWLEDGMENTS

This work is supported by the National Natural Science Foundation of China (Grants No. 61722403 and 11674121) and Jilin Province Science and Technology Development Program (Grant No. 20190201016JC). Calculations were performed in part at the high-performance computing center of Jilin University.

CONFLICT OF INTEREST

The authors declare no conflict of interest.

ORCID

Lijun Zhang https://orcid.org/0000-0002-6438-5486

REFERENCES

1. Helveg S, Lauritsen JV, Lægsgaard E, et al. Atomic-scale structure of single-layer MoS_2 nanoclusters. *Phys Rev Lett*. 2000;84:951-954.
2. Wang QH, Kalantar-Zadeh K, Kis A, Coleman JN, Strano MS. Electronics and optoelectronics of two-dimensional transition metal dichalcogenides. *Nat Nanotechnol*. 2012;7:699-712.
3. Szabo A, Koester SJ, Luisier M. Metal-dichalcogenide hetero-TFETs: are they a viable option for low power electronics? *72nd Device Research Conference*. Santa Barbara, CA, USA: IEEE; 2014:19-20.
4. Zhang L, Zunger A. Evolution of electronic structure as a function of layer thickness in group-VIB transition metal dichalcogenides: emergence of localization prototypes. *Nano Lett*. 2015;15:949-957.
5. Radisavljevic B, Radenovic A, Brivio J, Giacometti V, Kis A. Single-layer MoS_2 transistors. *Nat Nanotechnol*. 2011;6:147-150.
6. Ho W, Yu JC, Lin J, Yu J, Li P. Preparation and photocatalytic behavior of MoS_2 and WS_2 nanocluster sensitized TiO_2. *Langmuir*. 2004;20:5865-5869.
7. Bernardi M, Palummo M, Grossman JC. Extraordinary sunlight absorption and one nanometer thick photovoltaics using two-dimensional monolayer materials. *Nano Lett*. 2013;13:3664-3670.
8. Tsai ML, Su SH, Chang JK, et al. Monolayer MoS_2 heterojunction solar cells. *ACS Nano*. 2014;8:8317-8322.
9. Splendiani A, Sun L, Zhang Y, et al. Emerging photoluminescence in monolayer MoS_2. *Nano Lett*. 2010;10:1271-1275.
10. Tonndorf P, Schmidt R, Böttger P, et al. Photoluminescence emission and Raman response of monolayer MoS_2, $MoSe_2$,and WSe_2. *Opt Express*. 2013;21:4908-4916.
11. Scheuschner N, Ochedowski O, Kaulitz AM, et al. Photoluminescence of freestanding single- and few-layer MoS_2. *Phys Rev B*. 2014;89:125406.
12. Cai Y, Zhang G, Zhang YW. Polarity-reversed robust carrier mobility in monolayer MoS_2 nanoribbons. *J Am Chem Soc*. 2014;136:6269-6275.
13. Li Y, Xu CY, Zhang BY, Zhen L. Work function modulation of bilayer MoS_2 nanoflake by backgate electric field effect. *Appl Phys Lett*. 2013;103:033122.
14. Liu Q, Li L, Li Y, et al. Tuning electronic structure of bilayer MoS_2 by vertical electric field: a first-principles investigation. *J Phys Chem C*. 2012;116:21556-21562.

15. Avetisyan AA, Partoens B, Peeters FM. Electric field tuning of the band gap in graphene multilayers. *Phys Rev B*. 2009;79:035421.
16. Castro EV, Novoselov KS, Morozov SV, et al. Biased bilayer graphene: semiconductor with a gap tunable by the electric field effect. *Phys Rev Lett*. 2007;99:216802.
17. Kou L, Frauenheim T, Chen C. Nanoscale multilayer transition-metal dichalcogenide heterostructures: band gap modulation by interfacial strain and spontaneous polarization. *J Phys Chem Lett*. 2013;4:1730-1736.
18. Yun WS, Han SW, Hong SC, Kim IG, Lee JD. Thickness and strain effects on electronic structures of transition metal dichalcogenides: 2H-MX_2 semiconductors ($M = Mo, W; X = S, Se, Te$). *Phys. Rev. B*. 2012;85:033305.
19. Scalise E, Houssa M, Pourtois G, Afanas'ev V, Stesmans A. Strain-induced semiconductor to metal transition in the two-dimensional honeycomb structure of MoS_2. *Nano Res*. 2012;5:43-48.
20. Peelaers H, Van de Walle CG. Effects of strain on band structure and effective masses in MoS_2. *Phys Rev B*. 2012;86:241401.
21. Johari P, Shenoy VB. Tuning the electronic properties of semiconducting transition metal dichalcogenides by applying mechanical strains. *ACS Nano*. 2012;6:5449-5456.
22. Sharma M, Kumar A, Ahluwalia PK, Pandey R. Strain and electric field induced electronic properties of two-dimensional hybrid bilayers of transition-metal dichalcogenides. *J Appl Phys*. 2014;116:063711.
23. Conley HJ, Wang B, Ziegler JI, et al. Bandgap engineering of strained monolayer and bilayer MoS_2. *Nano Lett*. 2013;13:3626-3630.
24. He K, Poole C, Mak KF, Shan J. Experimental demonstration of continuous electronic structure tuning via strain in atomically thin MoS_2. *Nano Lett*. 2013;13:2931-2936.
25. Kou L, Du A, Chen C, Frauenheim T. Strain engineering of selective chemical adsorption on monolayer MoS_2. *Nanoscale*. 2014;6:5156-5161.
26. Lu N, Guo H, Li L, et al. MoS_2/MX_2 heterobilayers: bandgap engineering via tensile strain or external electrical field. *Nanoscale*. 2014;6:2879-2886.
27. Shi H, Pan H, Zhang YW, Yakobson BI. Quasiparticle band structures and optical properties of strained monolayer MoS_2 and WS_2. *Phys Rev B*. 2013;87:155304.
28. Das R, Mahadevan P. A model for the direct-to-indirect band-gap transition in monolayer $MoSe_2$ under strain. *Pramana*. 2015;84:1033-1040.
29. Yang L, Cui X, Zhang J, et al. Lattice strain effects on the optical properties of MoS_2 nanosheets. *Sci Rep*. 2014;4:1-7.
30. Fogler MM, Butov LV, Novoselov KS. High-temperature superfluidity with indirect excitons in van der Waals heterostructures. *Nat Commun*. 2014;5:1-5.
31. Wei XL, Zhang H, Guo GC, et al. Modulating the atomic and electronic structures through alloying and heterostructure of single-layer MoS_2. *J Mater Chem A*. 2014;2:2101-2109.
32. Georgiou T, Jalil R, Belle BD, et al. Vertical field-effect transistor based on graphene-WS_2 heterostructures for flexible and transparent electronics. *Nat Nanotechnol*. 2013;8:100-103.
33. Lee CH, Lee GH, Van Der Zande AM, et al. Atomically thin p-n junctions with van der Waals heterointerfaces. *Nat Nanotechnol*. 2014;9:676-681.
34. Ebnonnasir A, Narayanan B, Kodambaka S, Ciobanu CV. Tunable MoS_2 bandgap in MoS_2-graphene heterostructures. *Appl Phys Lett*. 2014;105:031603.
35. Schlaf R, Lang O, Pettenkofer C, Jaegermann W. Band lineup of layered semiconductor heterointerfaces prepared by van der Waals epitaxy: charge transfer correction term for the electron affinity rule. *J Appl Phys*. 1999;85:2732-2753.
36. Ma Z, Hu Z, Zhao X, et al. Tunable band structures of heterostructured bilayers with transition-metal dichalcogenide and MXene monolayer. *J Phys Chem C*. 2014;118:5593-5599.
37. Wang Q, Wu P, Cao G, Huang M. First-principles study of the structural and electronic properties of MoS_2—WS_2 and MoS_2—$MoTe_2$ monolayer heterostructures. *J Phys Appl Phys*. 2013;46:505308.
38. Kang J, Tongay S, Zhou J, Li J, Wu J. Band offsets and heterostructures of two-dimensional semiconductors. *Appl Phys Lett*. 2013;102:012111.
39. Yu Y, Hu S, Su L, et al. Equally efficient interlayer exciton relaxation and improved absorption in epitaxial and non-epitaxial MoS_2/WS_2 heterostructures. *Nano Lett*. 2015;15:486-491.
40. Su X, Cui H, Ju W, et al. MoS_2—MX_2 in-plane superlattices: electronic properties and bandgap engineering via strain. *Comput Mater Sci*. 2017;132:30-35.
41. Wang H, Wei W, Li F, Huang B, Dai Y. Step-like band alignment and stacking-dependent band splitting in trilayer TMD heterostructures. *Phys Chem Chem Phys*. 2018;20:25000-25008.
42. Zhou J, Kong X, Sekhar MC, et al. Epitaxial synthesis of monolayer $PtSe_2$ single crystal on $MoSe_2$ with strong interlayer coupling. *ACS Nano*. 2019;13:10929-10938.
43. Yamaoka T, Lim HE, Koirala S, et al. Efficient photocarrier transfer and effective photoluminescence enhancement in type I monolayer $MoTe_2/WSe_2$ heterostructure. *Adv Funct Mater*. 2018;28:1801021.
44. Butler SZ, Hollen SM, Cao L, et al. Progress, challenges, and opportunities in two-dimensional materials beyond graphene. *ACS Nano*. 2013;7:2898-2926.
45. Chhowalla M, Shin HS, Eda G, et al. The chemistry of two-dimensional layered transition metal dichalcogenide nanosheets. *Nat Chem*. 2013;5:263-275.
46. Nagao S, Fujimori T, Gotoh H, et al. Type-II photoluminescence from GaP/AlP/GaP quantum wells. *J Appl Phys*. 1997;81:1417-1421.
47. Kresse G, Joubert D. From ultrasoft pseudopotentials to the projector augmented-wave method. *Phys Rev B*. 1999;59:1758-1775.
48. Kresse G, Furthmüller J. Efficiency of ab-initio total energy calculations for metals and semiconductors using a plane-wave basis set. *Comput Mater Sci*. 1996;6:15-50.
49. Blöchl PE. Projector augmented-wave method. *Phys Rev B*. 1994;50:17953-17979.
50. Harl J, Kresse G. Accurate bulk properties from approximate many-body techniques. *Phys Rev Lett*. 2009;103:056401.
51. Sun Y, Wang X, Zhao XG, Shi Z, Zhang L. First-principle high-throughput calculations of carrier effective masses of two-dimensional transition metal dichalcogenides. *J Semicond*. 2018;39:072001.
52. Kang J, Zhang L, Wei SH. A unified understanding of the thickness-dependent bandgap transition in hexagonal two-dimensional semiconductors. *J Phys Chem Lett*. 2016;7:597-602.

53. Kośmider K, González JW, Fernández-Rossier J. Large spin splitting in the conduction band of transition metal dichalcogenide monolayers. *Phys Rev B*. 2013;88:245436.
54. Zeng H, Liu JB, Dai J, et al. Optical signature of symmetry variations and spin-valley coupling in atomically thin tungsten dichalcogenides. *Sci Rep*. 2013;3:1-5.
55. Yuan H, Bahramy MS, Morimoto K, et al. Zeeman-type spin splitting controlled by an electric field. *Nat Phys*. 2013;9:563-569.
56. Wang Z, Zhao D, Yu S, et al. First-principles investigation of structural and electronic properties of oxygen adsorbing phosphorene. *Prog Nat Sci Mater Int*. 2019;29:316-321.
57. Manzke R, Skibowski M. 2.7.3.1 Molybdenum dichalcogenides. In: Goldmann A, ed. *Subvolume B*. Vol 23. Berlin, Heidelberg: Springer-Verlog; 1994:131-141.
58. Al-Hilli AA, Evans BL. The preparation and properties of transition metal dichalcogenide single crystals. *J Cryst Growth*. 1972;15:93-101.
59. Liu L, Kumar SB, Ouyang Y, Guo J. Performance limits of monolayer transition metal dichalcogenide transistors. *IEEE Trans Electron Devices*. 2011;58:3042-3047.
60. Chiu MH, Zhang C, Shiu HW, et al. Determination of band alignment in the single-layer MoS_2/WSe_2 heterojunction. *Nat Commun*. 2015;6:1-6.
61. Ellis JK, Lucero MJ, Scuseria GE. The indirect to direct band gap transition in multilayered MoS_2 as predicted by screened hybrid density functional theory. *Appl Phys Lett*. 2011;99:261908.
62. Britnell L, Ribeiro RM, Eckmann A, et al. Strong light-matter interactions in heterostructures of atomically thin films. *Science*. 2013;340:1311-1314.
63. Shi Z, Wang X, Sun Y, Li Y, Zhang L. Interlayer coupling in two-dimensional semiconductor materials. *Semicond Sci Technol*. 2018;33:093001.
64. Ren H, Yu S, Cao L, et al. Efficient and stable Ruddlesden-Popper perovskite solar cell with tailored interlayer molecular interaction. *Nat Photonics*. 2020;14:154-163.
65. Li Y, Sun Y, Na G, Saidi WA, Zhang L. Diverse electronic properties of 2D layered Se-containing materials composed of quasi-1D atomic chains. *Phys Chem Chem Phys*. 2020;22:2122-2129.
66. Ceballos F, Bellus MZ, Chiu HY, Zhao H. Ultrafast charge separation and indirect exciton formation in a MoS_2—$MoSe_2$ van der Waals heterostructure. *ACS Nano*. 2014;8:12717-12724.
67. Matsui T, Seo JY, Saliba M, Zakeeruddin SM, Grätzel M. Room-temperature formation of highly crystalline multication perovskites for efficient, low-cost solar cells. *Adv Mater*. 2017;15:1606258.
68. Chen CY, Cheng CT, Yu JK, et al. Spectroscopy and femtosecond dynamics of type-II CdSe/ZnTe core-shell semiconductor synthesized via the CdO precursor. *J Phys Chem B*. 2004;108:10687-10691.
69. Zhang C, Chuu CP, Ren X, et al. Interlayer couplings, Moiré patterns, and 2D electronic superlattices in MoS_2/WSe_2 hetero-bilayers. *Sci Adv*. 2017;3:e1601459.
70. Kang J, Li J, Li SS, Xia JB, Wang LW. Electronic structural Moiré pattern effects on $MoS_2/MoSe_2$ 2D heterostructures. *Nano Lett*. 2013;13:5485-5490.
71. Liu L, Sun Y, Cui X, et al. Bottom-up growth of homogeneous Moiré superlattices in bismuth oxychloride spiral nanosheets. *Nat Commun*. 2019;10:1-10.

SUPPORTING INFORMATION

Additional supporting information may be found online in the Supporting Information section at the end of this article.

How to cite this article: Zhao X-G, Shi Z, Wang X, Zou H, Fu Y, Zhang L. Band structure engineering through van der Waals heterostructing superlattices of two-dimensional transition metal dichalcogenides. *InfoMat*. 2021;3:201–211. https://doi.org/10.1002/inf2.12155